Materials Today Bio 31 (2025) 101632

Contents lists available at ScienceDirect

Materials Today Bio

journal homepage: www.journals.elsevier.com/materials-today-bio

Chondroitin sulfate nanoparticles based on co-delivery dual drug induced ferroptosis in lung cancer cells by disrupting mitochondrial oxidative homeostasis

He Wang [a,b,1], Shuimu Lin [a,1], Jiacui Xie [a], Xuming Chen [a], Yating Deng [b], Pei Huang [b], Kanglong Peng [f], Wenhui Gao [c], Guodong Ye [a], Guihua Wang [e], Xiyong Yu [a], Huaying Wen [a,*], Linghao Qin [d,**], Yi Zhou [a,e,f,***]

[a] The Fifth Affiliated Hospital, Key Laboratory of Molecular Target and Clinical Pharmacology and the State Key Laboratory of Respiratory Disease, School of Pharmaceutical Sciences, Guangzhou Medical University, Guangdong 511436 Guangzhou, People's Republic of China
[b] The Second Affiliated Hospital, Guangzhou Medical University, Guangdong, 510260 Guangzhou, People's Republic of China
[c] Affiliated Cancer Hospital and Institue of Guangzhou Medical University, Guangdong, 510350 Guangzhou, People's Republic of China
[d] School of Pharmacy, Guangdong Pharmaceutical University, Guangzhou 510006, Guangdong, People's Republic of China
[e] Jiangzhong Pharmaceutical Co., LTD, Jiangxi, 330001 Nanchan, People's Republic of China
[f] Guangdong Yuewei Pharmaceutical Co., LTD, Guangdong, 515422 Jieyang, People's Republic of China

ARTICLE INFO

Keywords:
Chondroitin sulfate
Ferroptosis
Cinnamaldehyde
Curcumin
Mitochondrial REDOX homeostasis

ABSTRACT

Mitochondrial REDOX homeostasis is unbalanced by large amounts of reactive oxygen species production and reduced glutathione, leading to lipid oxidation-induced ferroptosis, which enhanced cancer immunotherapy. Thus, disrupting mitochondrial redox homeostasis represents a promising strategy for the treatment of lung cancer. In this study, a co-delivery system of based on chondroitin sulfate (CS) (CS-CA-CUR-TPP, CCCT) for natural medicines (Curcumin, CUR; and Cinnamaldehyde CA) was successfully constructed, which resulted in elevated ROS levels in cancer cells. Under the action of CS specifically targeting tumor cells, CCCT NPs is enriched and taken up by lung cancer cells. Acid responsiveness causes the CCCT NPs to break and escape from the lysosome, and CUR targets and destroys mitochondria under the action of mitochondrial target head triphenylphosphine (TPP). CA collaborates with CUR to produce large amounts of ROS and reduce GSH in a time-dependent manner in mitochondria for disruption of REDOX homeostasis, and triggers ferroptosis by reducing the expression of GXP4 and xCT proteins. The immunogenic cell death (ICD) after ferroptosis promotes interferon γ (IFN-γ), TNF-a, and IL-6 secretion. Our results desmontrat CCCT can promote inhibition of tumor growth by enhancing tumor immunogenicity. This study may provide a potential avenue for the advancement of self-delivery nanoparticles to overcome resistance to apoptosis in tumor therapy.

1. Introduction

Apoptosis is essential for maintaining homeostasis in multicellular organisms [1,2]. However, many tumor cells develop intrinsic or acquired resistance to pro-apoptotic therapies, leading to treatment failure and cancer recurrence [3–5]. In recent years, significant efforts have been directed toward exploring non-apoptotic cell death mechanisms, such as ferroptosis, to improve therapeutic outcomes for aggressive cancers [6]. Ferroptosis, an iron-dependent form of cell death, is triggered by the inhibition of glutathione peroxidase 4 (GPX4), disrupting the equilibrium between the generation and elimination of intracellular reactive oxygen species (ROS, predominantly hydroxyl radicals) [7,8]. The resulting ROS overproduction and accumulation elevate lipid peroxidation, initiating ferroptosis [9]. Unlike apoptosis, necroptosis, and

* Corresponding author.
** Corresponding author.
*** Corresponding author. The Fifth Affiliated Hospital, Key Laboratory of Molecular Target and Clinical Pharmacology and the State Key Laboratory of Respiratory Disease, School of Pharmaceutical Sciences, Guangzhou Medical University, Guangdong 511436 Guangzhou, People's Republic of China.
E-mail addresses: why3@vip.qq.com (H. Wen), qins_lab@163.com (L. Qin), zhouyi0264@126.com (Y. Zhou).
[1] He Wang and Shuimu Lin contributed equally to this work.

https://doi.org/10.1016/j.mtbio.2025.101632
Received 7 February 2025; Received in revised form 1 March 2025; Accepted 2 March 2025
Available online 5 March 2025

autophagy, ferroptosis not only suppresses tumor growth but also induces immunogenicity, offering a novel approach to overcoming apoptosis resistance [10,11].

Curcumin (CUR), a natural polyphenol derived from turmeric and related plants, has been shown to induce ferroptosis in cancer cells through multiple pathways. For instance, CUR activates autophagy [12] or upregulates HO-1 expression [13] in a dose-dependent manner to promote ferroptosis. Despite its potential, the high IC50 value of CUR limits its clinical applicability. Cinnamaldehyde (CA), a bioactive compound extracted from cinnamon, induces lipid oxidation by selectively targeting tumor cell mitochondria, generating high levels of ROS [14], Additionally, CA exhibits synergistic effects with berberine in suppressing lung cancer cell proliferation [15]. Based on these findings, we hypothesize that CA can enhance CUR's ability to induce ferroptosis in lung cancer and improve cancer immunotherapy. To address the limitations of CUR and CA, such as poor water solubility, low bioavailability, and limited selectivity, we propose developing a drug self-delivery system (DSDS) with low immunogenicity and high drug-loading efficiency [16]. However, DSDSs utilizing CUR and CA for ferroptosis-enhanced cancer immunotherapy remain largely unexplored.

Natural polymers, particularly polysaccharides, have gained significant attention in drug delivery due to their unique physicochemical and biological properties [17]. Chondroitin sulfate (CS), a naturally occurring glycosaminoglycan, is widely used in biomedical applications owing to its biodegradability, biocompatibility, low immunogenicity, and high water-binding capacity [18]. Notably, CS can target tumors by binding to CD44 receptors, which are overexpressed on the surface of various cancer cells [20], making it an ideal candidate for targeted drug delivery systems [19].

Lipophilic cations, characterized by their delocalized charge, are critical for mitochondrial targeting [20]. These compounds accumulate preferentially in the mitochondria of cancer cells due to the heightened negative membrane potential of cancer cell mitochondria [21]. Triphenylphosphonium (TPP), a commonly used lipophilic cation, is often employed to modify nanoparticles (NPs) or nanocarriers for mitochondrial-targeted drug delivery [22]. While promising, mitochondrial targeting alone is insufficient to address the growing challenge of tumor drug resistance [23].

In this study, we developed a novel ferroptosis-enhanced cancer immunotherapy strategy using biomimetic NPs. We first synthesized CUR-TPP by conjugating CUR with a mitochondrial-targeting TPP moiety. CUR-TPP and CA were then linked to CS via amide and acid-sensitive bonds, respectively, forming CA-CS-CUR-TPP (CCCT), which exhibits tumor-specific targeting. CCCT self-assembles into CS-based NPs in aqueous solutions. As outlined in Scheme 1, the key steps include: 1) prolonging circulation half-life to enhance drug exposure, 2) facilitating cellular uptake via CD44 receptors overexpressed on tumor cells, and 3) enabling rapid drug release through acid and enzyme-responsive mechanisms. In vitro and in vivo studies demonstrated that CCCT exhibits excellent biosafety, efficient tumor targeting, and enhanced anti-tumor efficacy. It directly induces ferroptosis by disrupting mitochondrial redox homeostasis and further amplifies cancer immunotherapy by activating immature dendritic cells (iDCs).

2. Methods

2.1. Materials

CUR and CA were supplied by Beijing Zeping Technology Co., Ltd. (Beijing, China). Chondroitin sulfate (CS), specifically type A with a molecular weight of 10 kDa, was sourced from Shandong Shoucheng Biotechnology Co., Ltd. (Shandong, China). This compound has the structure poly-1 (2/3)-N-acetyl-2-amino-2-deoxy-3-O-β-D-glucopyranurosyl-4-sulfonyl-D-galactose, characterized by a sulfonyl sulfation pattern. TPP and potassium iodide were sourced from Shanghai Xubang Pharmaceutical Technology Co., Ltd. Lyso Tracker Green was provided by Yeasen Biotech Co., Ltd. (Wuhan, China). The following reagents were obtained from Beyotime Biotechnology Co., Ltd. (Shanghai, China): 2-(4-Amidinophenyl)-6-indolecarbamidine dihydrochloride (DAPI), Annexin V-FITC/PI Apoptosis Detection Kit, and methylthiazolyldiphenyltetrazolium bromide (MTT). All anti-mouse antibodies, such as FITC-conjugated CD11c, PE-conjugated CD80, APC-conjugated CD86, PD-L1 antibody (αPD-L1), and ELISA kits for TNF-α, IFN-γ, and IL-6, were provided by BioLegend. BODIPY C11581/591, the Annexin V/PI apoptosis detection kit, and RIPA lysis buffer were obtained from Invitrogen Life Technologies. The β-actin antibody, xCT antibody, and GPX4 antibody were sourced from Cell Signaling Technology. The GSH/GSSG assay kit was procured from Beyotime. The near-infrared (NIR) fluorescent dye DIR was obtained from Keygen Biotech

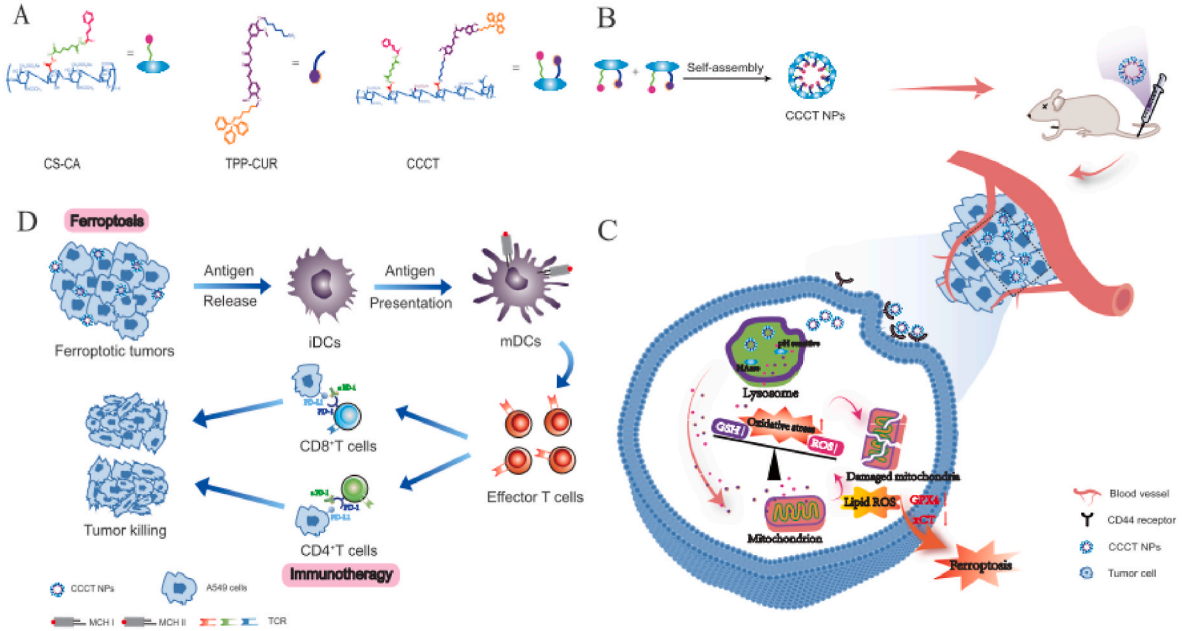

Scheme 1. The schematic illustration of synthesis of CCCT (A), preparation CCCT NPs (B), induction of ferroptosis (C), and ferroptosis-enhanced immutherapy (D).

(product code KGMP0026, based in China). The hematoxylin and eosin (H&E) staining kit was provided by Leagene Biology Technology Co., Ltd. (Beijing, China). LysoTracker ® Red and MitoTracker were obtained from Yeasen Biotech Co., Ltd. (Shanghai, China). Milli-Q water was used in all experiments.

2.2. Synthesis of CCCT (Fig. 1)

2.2.1 Synthesis of CS-CA: **①Synthesis of CS-Adipic dihydrazide (ADH):** At room temperature, 1.1 g of CS and 2.0 g of ADH were dissolved in 10 mL of distilled water and stirred for an additional 30 min. Hydrochloric acid was subsequently used to adjust the pH to a range of 4.70–4.75. Following this, 1.0 g of 1-ethyl-3-(3-dimethylaminopropyl) carbodiimide (EDC) was introduced into the solution, and the reaction proceeded for 48 h under magnetic stirring conditions. The resulting mixture was dialyzed for 48 h and subsequently lyophilized, yielding a white powder of CS-ADH with an efficiency of 89.75 %.**②Synthesis of CS-CA:** To prepare the CS-CA compound, 500 mg of CA was first dissolved in 5 mL of DMSO. This solution was then slowly incorporated into an aqueous solution containing 500 mg of CS-ADH while stirring. The mixture was reacted at ambient temperature for a period of 48 h. Following this, dialysis was performed using a molecular weight cutoff dialysis membrane, with a dialysate consisting of a 4:1 (v/v) distilled water and ethanol mixture. Gradually, the dialysate was exchanged with ultrapure water (pH adjusted to 7.0). Finally, the CS-CA product was obtained through freeze-drying, achieving a yield of 85.25 %.

2.2.2 Synthesis of TPP-CUR: **①Synthesis of CUR-BR:** A suitable quantity of CUR was introduced into a round-bottom flask along with anhydrous acetonitrile, and the mixture was stirred magnetically until complete dissolution. Subsequently, 0.14 g of anhydrous potassium carbonate powder and 0.2 g of potassium iodide as a catalyst were incorporated. The solution was then heated in an oil bath at 60 °C and allowed to reflux for 1 h. Following this, 1,6-dibromohexane (BR) was added, and the reaction was continued overnight. Thin-layer chromatography (TLC) was employed to monitor the progress of the reaction, using a petroleum ether to ethyl acetate ratio of 3:1. The final product, CUR-BR, was isolated with a yield of 48.11 %. **②Synthesis of BOC-CUR-BR:** To prepare BR-CUR-BOC, 0.1 g of CUR-BR was first dissolved in 10 mL of acetonitrile. Next, 0.052 g of potassium carbonate (K2CO3) was introduced into the solution, and the mixture was heated to 60 °C with reflux stirring for 30 min. Following this, 0.132 g of (6-bromohexyl)amino carboxylic acid tert-butyl ester (BOC), which is 2.5 times the molar amount of CUR-BR, was added to the reaction mixture. The solution was then stirred overnight while being monitored by thin-layer chromatography (TLC) using a petroleum ether:ethyl acetate (1:1) solvent system. The final product, BR-CUR-BOC, was obtained with a yield of 62.59 %. **③Synthesis of BOC-CUR-TPP:** To prepare TPP-CUR-BOC, 0.1 g of BR-CUR-BOC was first dissolved in 10 mL of acetonitrile. Subsequently, 0.114 g of potassium iodide (KI) was added to the solution, which was then heated to 85 °C. The mixture was stirred under reflux conditions for 30 min. After this period, 0.143 g of TPP, which is three times the stoichiometric amount required, was introduced into the reaction mixture and stirring was continued overnight. The reaction's progression was tracked using TLC, with a solvent system consisting of dichloromethane and methanol in a ratio of 10:1. The final product, TPP-CUR-BOC, was isolated in a yield of 70.39 %.

2.2.3 Synthesis of CUR-TPP: A suitable quantity of TPP-CUR-BOC was introduced into a mixture of TFA and DCM at a 1:1 ratio. The reaction mixture was stirred for 1.5 h. Subsequently, the solvents DCM and TFA were eliminated through rotary evaporation. A minimal volume of DCM was then added to solubilize the product, and TLC was employed to monitor the reaction progress using a DCM: MeOH ratio of 10:1. The final product, CUR-TPP, was isolated with a yield of 88.72 % (Fig. S1).

2.2.4 Synthesis of CA-CS-CUR-TPP (CCCT): At room temperature, 48 mg of CS-CA was dissolved in 10 mL of anhydrous N, N-dimethylformamide (DMF). Subsequently, 85 mg of DMTMM and 79.5 mg of DIPEA were added to the solution under mechanical stirring. The mixture was allowed to activate for 30 min. Next, 50 mg of CUR-TPP was dissolved in 10 mL of anhydrous DMF and subsequently introduced into the CS-CA solution. The reaction mixture was stirred at room temperature for 48 h. To purify the product, dialysis was performed for 48 h. After freeze-drying, the final product, CA-CS-CUR-TPP (CCCT), was obtained as a yellow powder with a yield of 85.32 %. Following a similar procedure as illustrated in Fig. 1, control compounds including CS-CUR, CUR-TPP (CT), CA-CS-CUR (CCC), and CS-CUR-TPP (CCT) were also prepared.

2.3. Preparation and characterizations

CCCT has the ability to self-assemble into nanoparticles (NPs) in an aqueous environment. To prepare the NPs, 20 mg of freeze-dried CCCT was dispersed in distilled water and subjected to mechanical stirring at room temperature for 30 min. Using a similar procedure, NPs of CS-CA, CS-CUR, CCC, and CCT were also fabricated. The characteristics of these NPs, including their size, zeta potential, and stability, were evaluated by dynamic light scattering (DLS) after dispersing them in phosphate-buffered saline (PBS). Transmission electron microscopy (TEM, JEOL, JEM-1400PLUS) was employed to evaluate the morphological characteristics of the NPs. The quantification of CUR or CA was performed through high-performance liquid chromatography (HPLC) using equipment from Waters Corporation (Waltham, MA, USA). The loading efficiency (LE) and encapsulation efficiency (EE) of DOX were calculated using the following equations:

$$LE = \text{weight of CUR or CA in CCCT/weight of CCCT} \times 100\%$$

$$EE = \text{weight of CUR or CA in CCCT/weight of total CUR or CA} \times 100\%$$

2.4. In vitro drug release

CCCT NPs were incubated in either PBS buffer (pH 7.4, 1.5 mL) or acetate buffer (pH 5.0 or 6.0, 1.5 mL), with or without the addition of HAase enzyme, under constant stirring at 100 rpm. At predetermined time points, 2 mL aliquots of the incubation medium were withdrawn and replaced with an equal volume of fresh release medium. The release profiles of CUR and CA were analyzed using HPLC. The cumulative percentage of CUR and CA released was then calculated according to the following formula:

The cumulative release of CUR and CA was determined as follows:
Percentage of release (%) = R1/R0 × 100%

R1: representing the weight of the released drug.
R0: representing the weight of the total drug in the nanocarrier.

2.5. Cell culture

Human lung adenocarcinoma cell lines (A549 and H226 cells), were procured from the College of Pharmaceutical Science at Guangzhou Medical University (Guangzhou, China). These cells were maintained in RPMI 1640 medium supplemented with 10 % fetal bovine serum (FBS), 100 units/mL penicillin, and 100 μg/mL streptomycin. All experiments involving cell cultures adhered to the guidelines established by the Institutional Animal Care Committee and Ethics Committee of Guangzhou Medical University (GZMUC 10–05010).

2.6. Mechanism of cellular endocytosis

A549 cells were seeded in 6-well plates at a density of 10^5 cells per well and incubated for 12 h. Following this incubation period, the cells were washed with PBS. The existing culture medium was replaced with

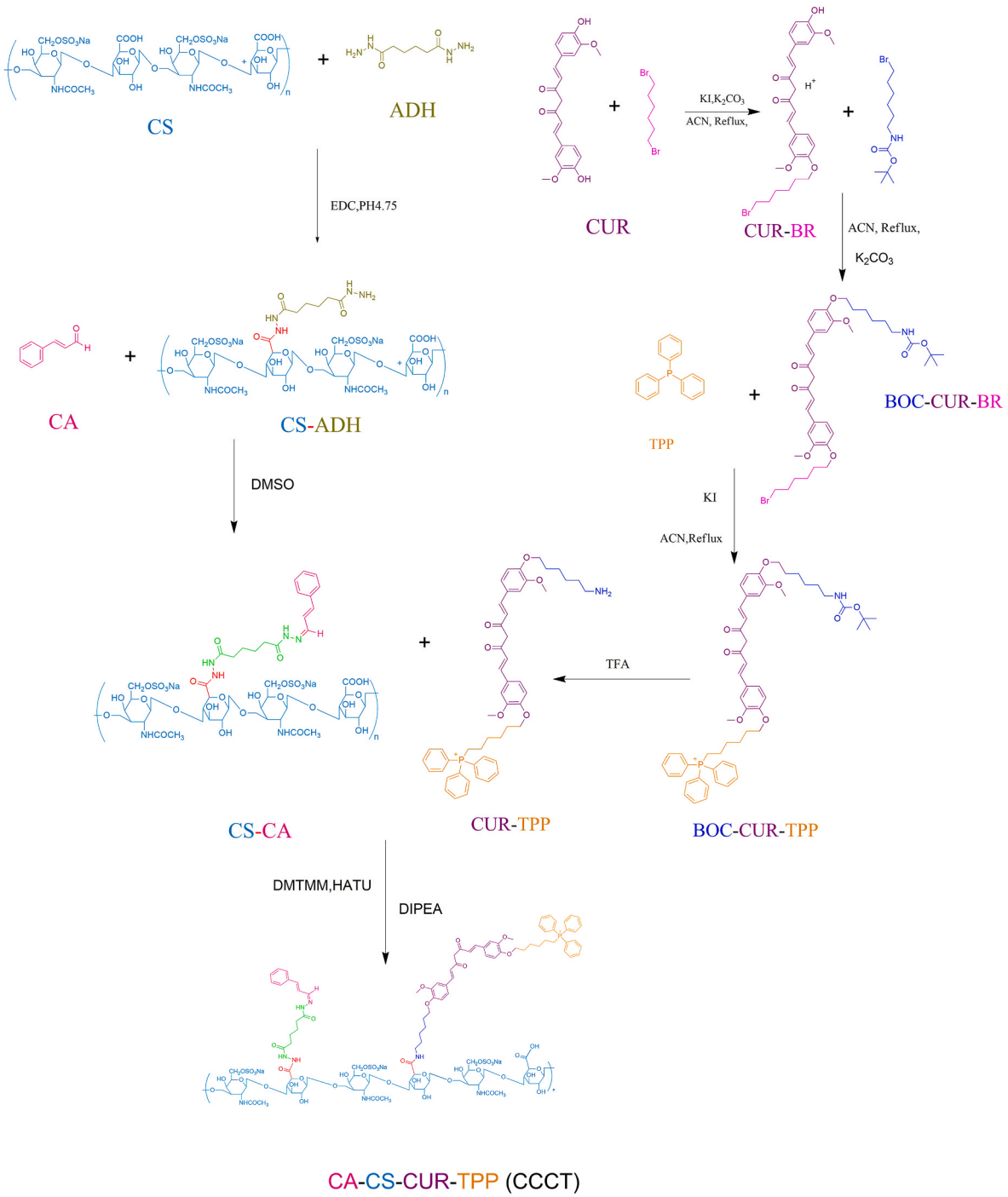

Fig. 1. Synthesis of CCCT.

fresh RPMI 1640 medium containing 1 mmol/L of 5-(N-ethyl-N-isopropyl)-amiloride, 10 mg/mL of chlorpromazine, and 200 mmol/L of genistein, and the cells were incubated in this medium for 30 min. Next, the cells were exposed to CCCT NPs (with CUR concentration at 3.05 μg/mL and CA concentration at 1.92 μg/mL) for 2 h at 37 °C. After treatment, the cells were rinsed three times with cold PBS. Confocal laser scanning microscopy (CLSM) was then used to image the A549 cells, utilizing an Olympus FV1000 system located in Central Valley, PA, USA.

2.7. Lysosome escape

A549 cells were seeded at a density of 5 × 10^4 cells per well in a specialized confocal microscopy dish (NEST). After a 24-h incubation, the cells were treated with CCCT NPs (CUR: 3.05 μg/mL, CA: 1.92 μg/mL) for 1, 3, or 6 h. Following the treatment, the cells were stained with LysoTracker Red (1 mM) for 30 min and DAPI (2 mg/mL) for 10 min under dark conditions at 37 °C. The cells were then washed with cold PBS and subsequently imaged using CLSM.

2.8. Mitochondria localization

A549 cells were seeded in an 8-well chamber slide (Lab-Tek) at a density of 1.5 × 10^4 cells per well. These cells were then exposed to CCCT NPs, with concentrations of CUR at 3.05 μg/mL and CA at 1.92 μg/

mL, for a period of 8 h. For mitochondrial visualization, MitoTracker Blue was applied at a concentration of 1 μM, while LysoTracker Red was used at the same concentration to visualize lysosomes. Cellular imaging was conducted using CLSM.

2.9. Cytotoxicity and hemo-compatibility of NPs in vitro

A549 and H226 cells were seeded into separate wells of a 96-well plate at a density of 10,000 cells per well. Following a 12-h incubation period, the existing growth medium was replaced with fresh medium containing various types of nanoparticles (NPs). The control group contained only the standard culture medium. Cell viability was evaluated at 24, 48, and 72 h using the MTT assay [24]. The findings were derived through the use of a microplate reader, and the IC50 values for the various groups were determined. The particular equation utilized is presented below:

$$\text{Inhibition rate} = [(\text{Ac-As})/(\text{Ac-Ab})] \times 100\%$$

Ac: Absorbance of experimental group.
As: Absorbance of control group.
Ab: Absorbance of blank group.

The IC50 was then calculated by GraphPad Prism 8 on the basis of the obtained inhibition rate.

The synergistic effects between CA and CUR in the CCCT NPs was evaluated by the following Eq. (2) [25];

$$\text{CI}=\text{CUR } 1/\text{CA } 0 + \text{CUR } 1/\text{CA } 0 \quad (2)$$

Where CI is combination index, CA 1 and CUR 1 represent the IC 50 values of drugs used in the combination treatment, and CA 0 and CUR 0 represent the IC 50 values of the single drugs. CI < 1 indicates drug synergism, whereas CI > 1 shows an antagonistic effect.

2.10. Hemo-compatibility of the nanomedicines in vitro

The hemo-compatibility of nanomicelles was examined using the protocol described in Ref. [26]. A 50 μL aliquot of red blood cell (RBC) suspension was gently introduced into 1 mL of PBS containing different concentrations of CCCT (ranging from 0 to 50 μg/mL, specifically 0, 0.01, 0.1, 1, 10, 20, 30, 40, and 50 μg/mL). After an overnight incubation period, the RBC suspension underwent centrifugation. Subsequently, the supernatants were collected and analyzed using a microplate reader. The formula for calculation is provided below:

$$\text{Hemolysis (\%)} = [(\text{As- An})/(\text{Ap- An})] \times 100\%$$

As, An, and Ap are the absorbance of the sample, negative and positive control samples, respectively.

2.11. JC1 assay

A549 cells were grown in an LabTek 8-well chamber slide. The cells, at a density of 1.5×10^4, were incubated with CCCT NPs (CUR concentration: 3.05 μg/mL, CA concentration: 1.92 μg/mL) for 12 h. A control group without nanoparticles was also maintained. Following incubation, the cells were rinsed twice with PBS (pH 7.4) and then stained with JC-1 dye (Beyotime Institute of Biotechnology, China), a mitochondrial membrane potential indicator, at a concentration of 10 μg/mL for 20 min at 37 °C. Prior to staining, cellular images were captured using CLSM with a fluorescence emission wavelength of 590 nm. To correct for baseline fluorescence, the red fluorescence emitted by the NPs was measured and subtracted from the JC-1 fluorescence signal. Finally, CLSM was utilized to visualize and quantify the JC-1 signal within the cells.

2.12. Biological electron microscopy observations

A549 cells were treated with CCCT NPs at concentrations equivalent to 3.05 μg/mL of curcumin (CUR) and 1.92 μg/mL of caffeic acid (CA). Following a 12-h incubation period, the cells were washed, collected, and fixed. The mitochondrial structure was then examined using biological electron microscopy. (PerkinElmer).

2.13. Western blotting

A549 cells were cultured in 6-well plates and treated with PBS, CUR, CUR combined with CA, CCT, CCC, and CCCT, all at equivalent concentrations of CUR (3.05 μg/mL) and CA (1.92 μg/mL). Following a 24-h incubation period, the cells were washed with PBS and subsequently lysed using RIPA buffer to extract proteins for western blot analysis.

2.14. DC stimulation experiment in vitro

In a study where dendritic cells (DCs) were stimulated in vitro, the DCs were isolated from female Balb/c mice aged 6–8 weeks, following a previously established protocol [27]. To ensure accuracy, the experiments were performed in quadruplicate. For the in vitro DC stimulation experiment, a 24-well transwell system with polycarbonate membranes containing 0.4 μm pores was utilized. Specifically, 10,000 A549 cells were placed in the upper chambers of this system. When these cells reached 70–80 % confluence, they were treated with CCCT (CUR: 3.05 μg/mL, CA: 1.92 μg/mL) along with Fer-1 (at a concentration of 10 μM) for 6 h. Following this, DCs were introduced into the lower chambers at a density of 5×10^4 cells per well and co-cultured with the contents from the upper chambers. To serve as controls, A549 cells were exposed to free CUR, CCT, CCC, and CCCT formulations, all containing equivalent concentrations of CUR or CA. Following co-incubation, the DCs were harvested and stained with a mixture consisting of 5 μL anti-CD11c FITC (eBioscience; 0.2 mg/mL), 5 μL anti-CD86 PE (eBioscience; 0.2 mg/mL), and 5 μL anti-CD80 APC (eBioscience; 0.2 mg/mL) for 15 min. The stained DCs were then subjected to centrifugation at 120×*g* for 5 min, re-suspended, and analyzed via flow cytometry. Post-treatment, cytokine levels, including TNF-α, IFN-γ, and IL-6, in the DC culture supernatants were quantified using ELISA kits (Invitrogen) according to the manufacturer's protocol.

2.15. In vivo imaging assay

Female BALB/c mice, aged 5 weeks and weighing between 16 and 18 g, were subcutaneously injected with A549 cells (1×10^7 cells suspended in 200 μL of PBS) on the right flank. When the tumor volumes grew to approximately 200–230 mm^3, the mice were administered either free DIR or DIR-loaded nanomicelles (CCCT/DIR) via intravenous injection, with a total volume of 100 μL. Images were acquired at specific time points (0, 2, 4, 8, 12, and 24 h) using an NIR fluorescence imaging system. Following the 24-h post-injection period, the mice were euthanized, and major organs were imaged for DIR signals. All animal procedures complied with the guidelines established by the Animal Care and Use Committee of Guangzhou Medical University.

2.16. Antitumor study and immune stimulation experiment in vivo

To establish the A549 tumor model, we followed the described protocol. Female BALB/c mice bearing A549 tumors were subsequently allocated into five groups (with five mice per group): PBS, CUR, CCT, CCC, and CCCT. Equimolar doses of CUR (1.52 mg/kg) and CA (0.95 mg/kg) were delivered intravenously every other day for a total of five administrations. Tumor volume and body weight were monitored bi-daily. Specifically, tumor volume was determined using the formula (width [2] × length):/2, and relative tumor volume was assessed by comparing measurements before and after treatment. On the third day

post-final administration, mice were euthanized in a humane manner to harvest heart, liver, spleen, lung, kidney, and tumor tissues for subsequent H&E staining and immunohistochemical examination.

The A549 tumor model was established following the previously described methodology. Mice successfully harboring A549 tumors were subsequently allocated into three groups (four mice per group): PBS control, CCCT treatment, and CCCT combined with intravenous administration of αPD-L1 (2 mg/kg). These dosages were equivalent to 0.25 mg/kg of CUR or 0.5 mg/kg of CA in molar terms. Tumor dimensions and body weights of the mice were documented every two days. Lymph nodes were harvested, mechanically dissociated, and suspended in 1 × PBS containing 2 % FBS to prepare single-cell suspensions. For assessing DC maturation, flow cytometry was employed to analyze the suspensions stained with anti-CD11c FITC, anti-CD86 PE, and anti-CD80 APC antibodies. Furthermore, serum levels of cytokines such as TNF-α, IL-6, and IFN-γ were quantified using ELISA kits, adhering to the manufacturer's protocols [28].

2.17. Statistics

The results are expressed as mean ± SD from at least three independent experiments. Statistical evaluations were performed using GraphPad Prism 8 software, utilizing either an unpaired Student's t-test or one-way ANOVA. Statistically significant differences were defined by

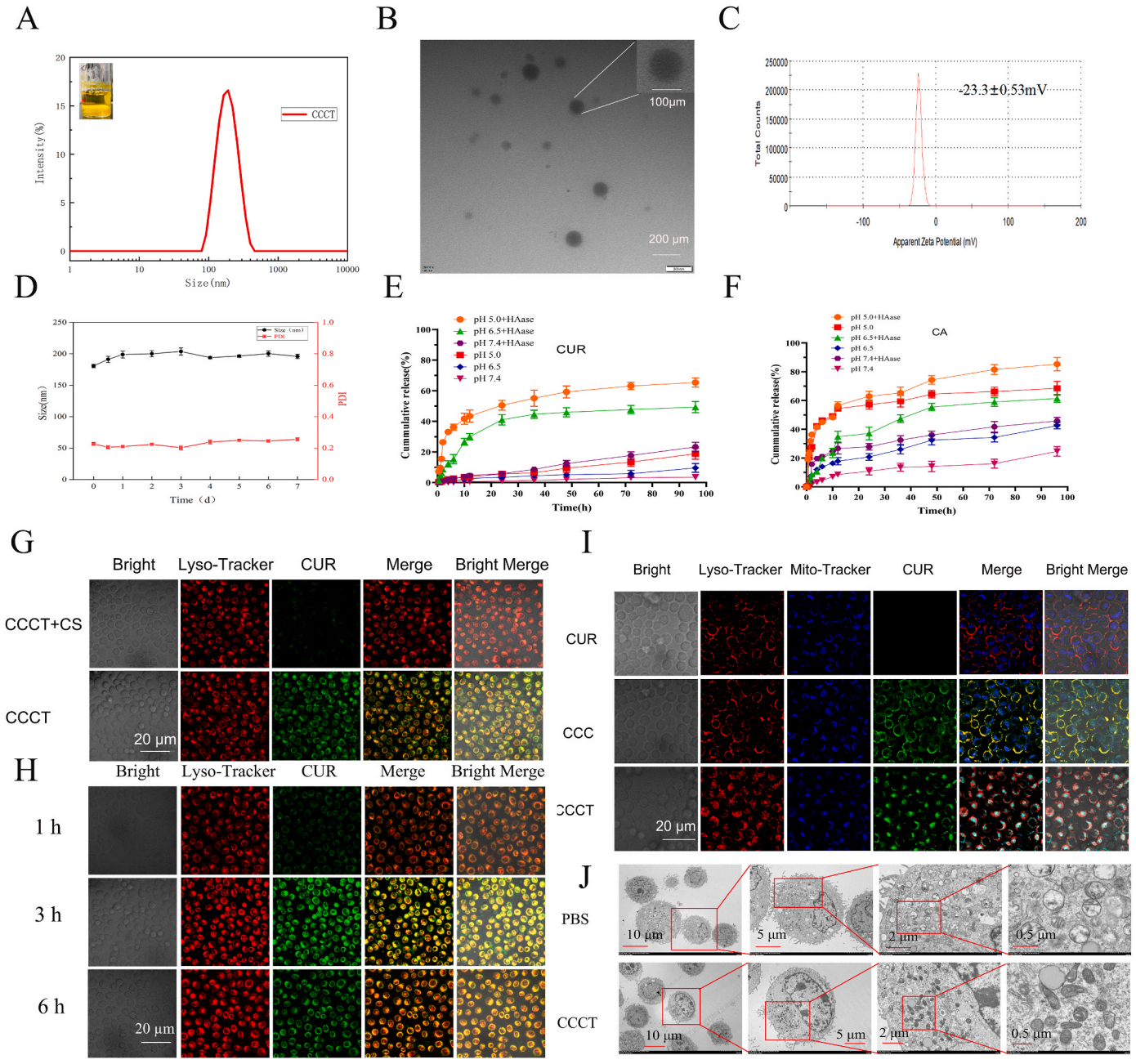

Fig. 2. Characterization of CCCT NPs. The size (A), zeta potential (B), and TEM image (C) of CCCT NPs, scale bar: 200 nm. (D) The size or PDI changes of CCCT NPs in during incubation in PBS containing 10 % FBS at 37 °C for 7 d. The CUR (E) or CA (F) release behaviors of CCCT NPs under the conditions of pH 7.4, pH 6.5 or pH 5.0 (with or without HAase) (n = 3). (G) CLSM images of A549 cells after 30 min of incubation with CCCT + CS and CCCT (n = 3). (H) Merge CLSM image showed lysosomes escape of CCCT NPs on A549 cells. The lysosomes were stained by LysoTracker Red. Green fluorescence indicated CUR. Yellow fluorescence indicated the overlay between CUR and lysosomes. (I) Co-localization of the CUR, CUR + CA, CCC, and CCCT into mitochondria at A549 cells at 24 h observed by CLSM. The mitochondria were stained by MitoTracker Red. (J) TEM image of mitochondria after PBS and CCCT NPs treated on A549 cells for 24 h.

a significance level of $p < 0.05$, $p < 0.01$, or $p < 0.001$.

3. Results and discussion

3.1. Characteristics of CCCT NPs

The successful synthesis of CCCT was initially confirmed by ^{1}HNMR, where a peak at 1.8 ppm (-CH_3-) corresponding to CS was observed, while the peaks at 1.54 ppm and 2.21 ppm (-CH_2-) were assigned to ADH. Additionally, the hydrogen signals in Benzene were observed at 7.23 ppm and 7.42 ppm for CA, 6.66 ppm and 7.81 ppm for CUR, and finally at 7.73 ppm for TPP, respectively, indicating successful synthesis of CCCT (Fig. S2).

The successful synthesis of CCCT was further confirmed by infrared spectroscopy. A characteristic hydroxyl peak is observed at 3420 cm^{-1}, while characteristic benzene ring peaks are detected at 817 cm^{-1}, 841 cm^{-1}, 765 cm^{-1}, and 720 cm^{-1}. Additionally, a distinctive urea bond peak appears at 1705 cm^{-1}. Notably, an enhanced absorption peak emerges at 1568 cm^{-1} as a newly formed characteristic amide bond peak, providing further confirmation of the successful synthesis of CCCT (Fig. S3). The results of UV–vis spectrum in Fig. S4 show that the ultraviolet absorption peak of CA in compound CS-CA is observed at 310 nm, which differs from the intrinsic ultraviolet absorption peak of CA itself at 290 nm. This discrepancy can be attributed to the red shift resulting from the formation of a hydrazine bond, thereby indicating the successful synthesis of CS-CA. The UV absorption peak of CUR in CUR-TPP was observed at 377 nm, which exhibited a disparity from the corresponding UV absorption peak of CUR itself at 430 nm. It may be that the -NH_2 group causes the blue shift in the spectrum. CCCT compounds displayed absorption peaks at 310 nm and 377 nm, which corresponded to the characteristic absorption peaks of CA and CUR-TPP, respectively, providing further evidence for the successful synthesis of CCCT.

The drug loading efficiencies of CA and CUR were quantified as 5.60 % and 8.97 %, respectively, utilizing high-performance liquid chromatography (HPLC). The standard curves are presented in Fig. S5. The hydrodynamic diameter of CCCT NPs was found to be 196.02 ± 6.3 nm (Fig. 2A), indicating a narrow size distribution and excellent dispersion in the aqueous phase. In addition, due to the modification of CS, the potential of CCCT is controlled at −23.3 mv, which is more conducive to its long circulation in the body (Fig. 2B). The hemocompatibility test in mice further demonstrated the enhanced safety of CS-modified CCCT (Fig. S6). As depicted in Fig. 2C, the fabrication of CCCT NPs resulted in the formation of uniformly spherical nanoparticles by TEM. In addition, we observed that the particle size and PDI barely changed over a long period of time, suggesting that CCCT NPs has a good stability (Fig. 2D, Fig. S7). The results of this study highlight the significant advantages of employing the self-assembly approach in the development of NPs for biomedical applications [29].

The acidic tumor microenvironment facilitates the efficient drug release of acid responsive NPs [16]. The release of CA and CUR in CCCT was assessed in this experiment (Fig. 2E–F). The cumulative release rates of CA and CUR from CCCT NPs were found to be below 30 % at pH 5.0 after 2 h, respectively. Even under the influence of HAase at pH 5.0, the cumulative release rates of both drugs only reached approximately 35 %, indicating that CCCT NPs did not exhibit abrupt release behavior. The cumulative CA release rates of CCCT NPs at pH 7.4, pH 6.5, and pH 5.0 without HAase after 96 h were found to be significantly higher (24.79 %, 45.92 %, and 69.41 % respectively) compared to the release rates of CUR (3.34 %, 9.72 %, and 18.30 % respectively), indicating a pronounced response to acid-sensitive bonds. Upon addition of HAase, the cumulative release of CA and CUR increased in their respective pH environments. Specifically, the CA values were 42.69 %, 61.87 %, and 85.88 %, while the CUR values were 23.20 %, 49.20 %, and 65.75 %. This result further demonstrates the effective dissolution of the CCCT NPs shell (HA) by HAase, leading to rapid decomposition of the hydrophobic core and early release of CA in response to acid.

3.2. Cellular targeting, uptake and subcellular distribution of CCCT NPs

Tumor cell targeting significantly enhances the therapeutic efficacy of drug formulations [23]. To investigate the tumor cell targeting ability of CCCT NPs, we incubated A549 cells with both free CS and CCCT NPs for a duration of 12 h. As depicted in Fig. 2G, the introduction of free CS results in a significant reduction in the uptake of CCCT NPs by A549 cells, as observed through CLSM analysis, when compared to CCCT alone. This phenomenon can be attributed to the competitive binding between free CS and CD44 molecules that are highly expressed on the surface of tumor cell membranes, indicating that CCCT exhibits CD44-mediated targeting towards tumor cells. The mechanism of CCCT uptake was subsequently investigated. Fig. S8 showed colchicine, chloroquine, and chlorpromazine exhibited varying degrees of inhibition on the endocytosis of CCCT NPs when compared to the PBS group. However, their inhibitory abilities were not identical, with chloroquine and chlorpromazine demonstrating a more pronounced inhibitory effect. The findings revealed that the internalization of CCCT NPs predominantly occurred via clathrin-mediated endocytosis and endosome maturation-dependent endocytosis.

After cellular internalization, the majority of drugs are sequestered within lysosomes. To assess the lysosomal escape capability of CCCT NPs, we employed the Lyso-Tracker Red probe as an experimental tool. The yellow color observed when the red fluorescence of the lysosome fully overlapped with the green fluorescence of the CUR indicates a high degree of colocalization, which is positively correlated with the intensity of yellow light. The results are presented in Fig. 2H. At 1 h, the green fluorescence of cells in each treatment group exhibited weak intensity, indicating incomplete lysosomal entry of the drug at that time point. In contrast, at the 3 h, CCCT nanoparticles exhibited the most intense green fluorescence that overlapped with the red fluorescence of lysosomes, resulting in a bright golden yellow color. This indicates a high degree of colocalization between CCCT nanoparticles and lysosomes. By 6 h, the intensity of the golden yellow color had diminished, and an increased amount of green fluorescence was observed outside the red-stained lysosomes, suggesting that a greater proportion of acid-released drugs had escaped from the lysosomal compartment.

3.3. Colocalization and membrane permeabilization in the mitochondria

After the escape of CA and TPP-CUR from lysosomes, TPP-CUR will utilize TPP for mitochondrial targeting and subsequent release of chemotherapeutic agents within the mitochondria. The Mito-Tracker Red probe was employed as an experimental tool. The green fluorescence of CS-CA, CT, CCC, and CCCT groups exhibited a progressive enhancement as observed through CLSM in Fig. 2I. This can be attributed to the following reasons: 1) The absence of CUR drug in the CS-CA group; 2) Limited cellular uptake of CT due to its hydrophobic nature and poor solubility; 3) Selective targeting and concentration on tumor cells facilitated by CS in both CCC and CCCT groups. Among them, the green fluorescence of CCCT NPs was highly coincident with the blue fluorescence of Mito-Tracker, resulting in a cyan coloration that suggests accurate mitochondrial targeting of most CUR drugs within the TPP target. The overlapping regions of CCC NPs exhibit a yellow-green fluorescence, accompanied by a slight cyan fluorescence, indicating the predominant cytoplasmic localization of CCC NPs.

When a drug acts on the mitochondria, it induces morphological changes in mitochondrial structure, depolarization of the mitochondrial membrane potential, increased cells membrane permeability, and so on [30]. Fig. 2J showed the mitochondrial membrane becomes denser, the volume shrinks, the outer membrane ruptures, and the mitochondrial cristae decrease or disappear in CCCT group, compared with PBS group, indicated cancer cells ferroptosis was found. The PBS group exhibited enhanced red fluorescence and weak green fluorescence, as illustrated in

Fig. S9, indicating a high mitochondrial membrane potential at this stage. Moreover, JC-1 remains condensed within the mitochondria, suggesting that cellular mitochondria remain undamaged. In contrast, CCCT NPs exhibited contrasting results, with a significant reduction in red fluorescence and a notable enhancement in green fluorescence. These findings indicate a decline in mitochondrial membrane potential and impairment of mitochondrial function, suggesting CCCT NPs may induce mitochondrial damage.

3.4. Anti-proliferation effects of CCCT NPs

Cell viability assays were performed to evaluate the effects of CA, CUR, CA + CUR, CS-CA, CS-CUR, CT, CCT and CCC at 24, 48 and 72 h. The experimental results showed that the survival rate of cells decreased to different degrees with different substances (Fig. 3A). CCCT NPs exhibited the most potent antitumor activity at 24, 48, and 72 h, compared with other groups. The IC50 values of A549 cells treated with CCCT NPs were 9.82, 2.76, and 1.22 μM at above three time points, respectively. CCCT NPs' IC50 values decreased by 22.1 %–67.2 % compared to CCC NPs, and by 33.8 %–79.2 % compared to CCT NPs, suggesting that not only mitochondrial targeting improved the therapeutic effect, but also that CA synergically expanded CUR to inhibit the proliferation of lung cancer cells. The ratio of CUR to CA in CCCT NPs (1.5/1, w/w) showed a strong inhibitory effect on A549 cell proliferation, which consistent results with our previous findings (Fig. S10). The observed synergistic effect was further supported by the calculated combination index (CI) values, which were less than 1 for both A549 (0.68) and H226 (0.74).

GSH, a highly prevalent antioxidant in cells that require oxygen, has the potential to function as a scavenger of free radicals and an inhibitor of lipid peroxidation [31,32]. This ability helps protect cellular components from damage caused by ROS. Disturbances in GSH metabolism

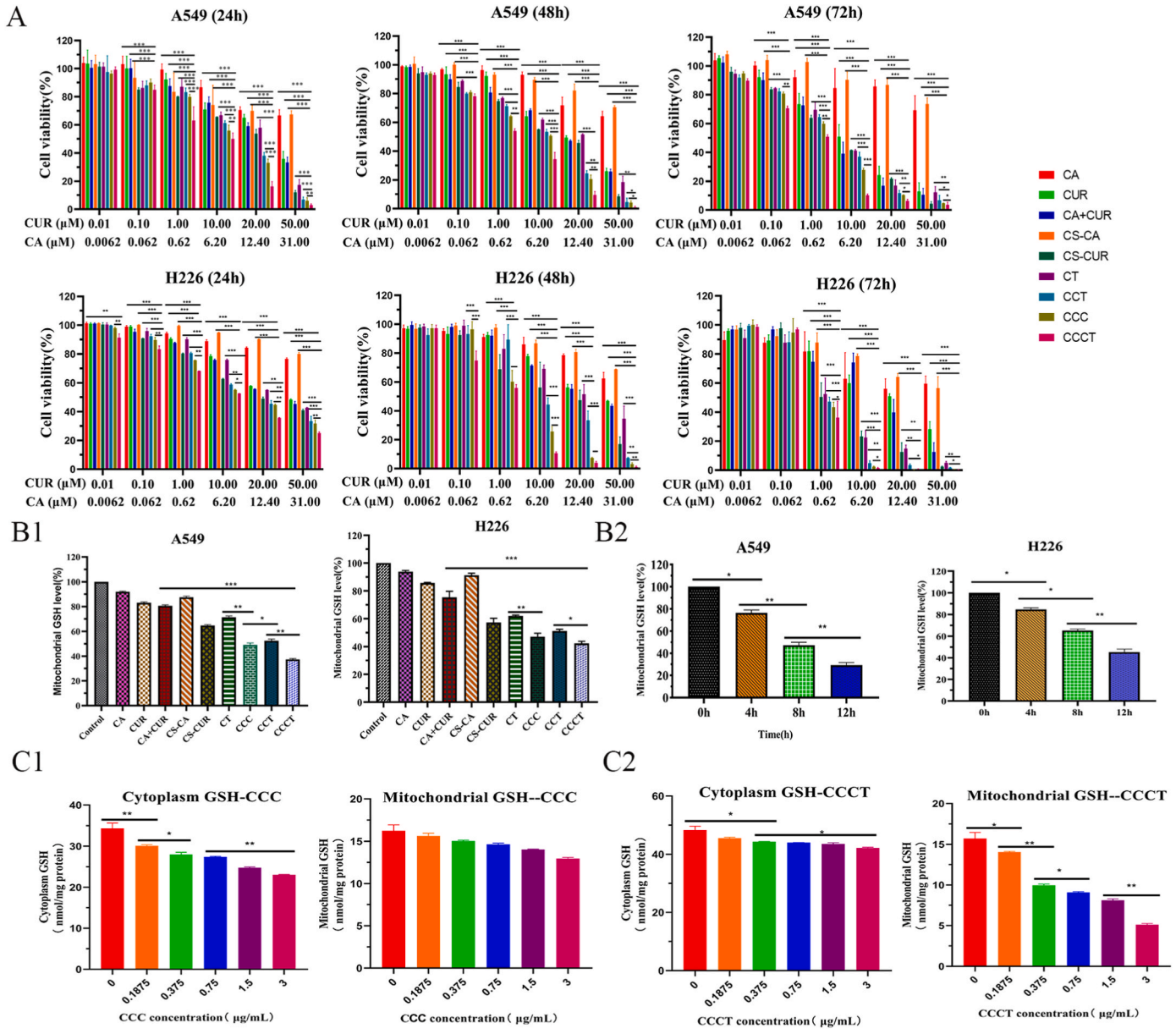

Fig. 3. The enhanced antitumor activity of CCCT NPs. (A) Cytotoxicity of PBS, CUR, CA, CUR + CA, CS-CA, CS-CUR, CT, CCC, CCT, and CCCT in lung cancer A549 and H226 cells after incubation for 24, 48, and 72 h (n = 6). (B1) The level of GSH in mitochondria of A549 cells treated with different drug groups for 12 h (n = 3). (B2) The level of GSH in mitochondria of CCCT NPs in A549 cells at different time points (n = 3). The level of GSH in mitochondria and cytoplasm of A549 cells treated with different does CCC (C1) or CCCT (C2) for 12 h (n = 3). All data are presented as the means ± standard deviations; *P < 0.05, **P < 0.01, ***P < 0.001.

have been linked to the development of cancer, with various tumors exhibiting elevated levels of GSH [32]. As depicted in Fig. 3B1, treatment with CUR, CA, CUR + CA, CS-CUR, CT, CCT, and CCC NPs led to approximately 15 %–52 % reductions in mitochondrial GSH levels, respectively. The CCCT NPs, in contrast, exhibited a significant reduction to 68 %, which was notably lower compared to the other treatments previously employed, owing to their specific mitochondrial targeting or the combination of two drugs. Furthermore, as the incubation time was prolonged, there was a gradual decrease in the level of mitochondrial GSH in CCCT group, indicating an enhanced capacity for mitochondrial GSH consumption. This phenomenon can be attributed to the drug's initial localization within lysosomes at 3 h and subsequent translocation to mitochondria after 6 h. The depletion of mitochondrial GSH persisted for 12 h (Figs. 3B–2). The observed phenomenon stands in stark contrast to the CCC group (Fig. 3C), as CCCT NPs exhibit targeted mitochondrial localization and exert their effects therein, thereby inducing substantial mitochondrial ROS generation.

The ability of CCCT NPs to induce mitochondrial ROS production in lung cells was examined using a fluorescent ROS probe (DHE) and visualized by CLSM. To confirm the mitochondrial origin of ROS, Mito-Tracker was used to stain the mitochondria of both A549 and H226 cells. As shown in Fig. 4A–B, intracellular ROS levels were significantly higher in the CCCT group compared to other groups in both cell lines. Compared to CCC and CCT NPs, the CCCT NPs exhibited the most pronounced colocalization with the blue fluorescence of Mito-Tracker, appearing as a pink signal. Additionally, Fig. 4C demonstrates a time-dependent characteristic in terms of the overlap between the red and blue fluorescence signals in the CCCT group, wherein an increase in incubation time leads to a gradual augmentation of this overlap (12 h). This observation suggests that ROS generation induced by CCCT NPs primarily occurs within mitochondria, thereby providing further evidence for their mitochondrial targeting and CA synergistic therapy.

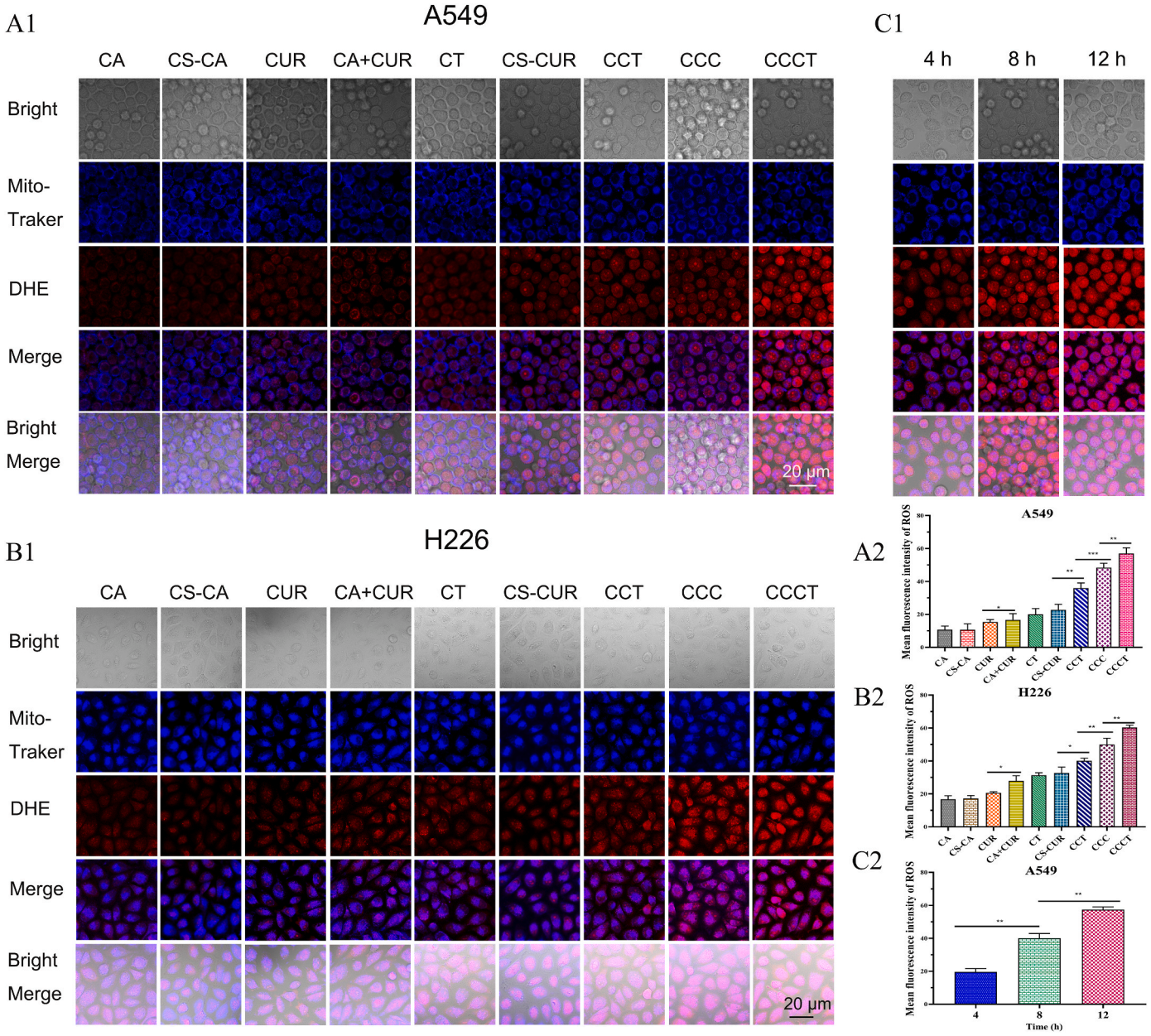

Fig. 4. CCCT NPs induced REDOX homeostasis imbalanced. (1) Fluorescence images and (2) corresponding fluorescence intensity of ROS in A549 cells (A) and H226 (B) treated with different administration groups for 12 h (C1) Fluorescence images and (C2) corresponding fluorescence intensity of ROS production of CCCT NPs in A549 cells at different time points. All data are presented as the means ± standard deviations (n = 3); *P < 0.05, **P < 0.01, ***P < 0.001.

3.5. Study on ferroptosis and its mechanism

ROS production and subsequent hydroxyl radical (·OH) mediated lipid peroxidation ultimately lead to plasma membrane damage resulting in ferroptosis [33]. In order to investigate the activation of the ferroptosis mechanism and induction of tumor cell death by CCCT NPs, two different ferroptosis inhibitors, DFO and Fer-1, were separately added to CCCT and incubated with tumor cells for 24 h. The results demonstrated that the inclusion of DFO and Fer-1 attenuated the cytotoxicity of CCCT NPs towards tumor cells, indicating a potential reversal effect on CCCT-induced cell death. Notably, this reversal effect exhibited concentration-dependent characteristics. Fig. 5A shows that when different doses of DFO were added, the cell survival rate in the DFO + CCCT group increased from 35 % without any addition (only CCCT) to the highest 54 %. When replacing DFO with FER, the maximum rises to 60 % (Fig. 5B). The same findings were also noted in H226 cells (Fig. 5C–D). Meanwhile, in comparison to the PBS group, CUR, CUR + CA, CCT, CCC, and CCCT NPs exhibited a different extent of down-regulation of ferroptosis signature proteins GPX4 and xCT (Fig. 5E–F). The most significant down-regulation was observed in the CCCT group. Furthermore, we observed apoptosis in A549 cells induced by varying concentrations of CCCT NPs and noted that the apoptosis rate remained below 25 %, indicating that CCCT-induced cell death primarily occurred through other pathway (Fig. S11). These findings suggest that ferroptosis is mainly implicated in lung cancer cell death mediated by CCCT NPs.

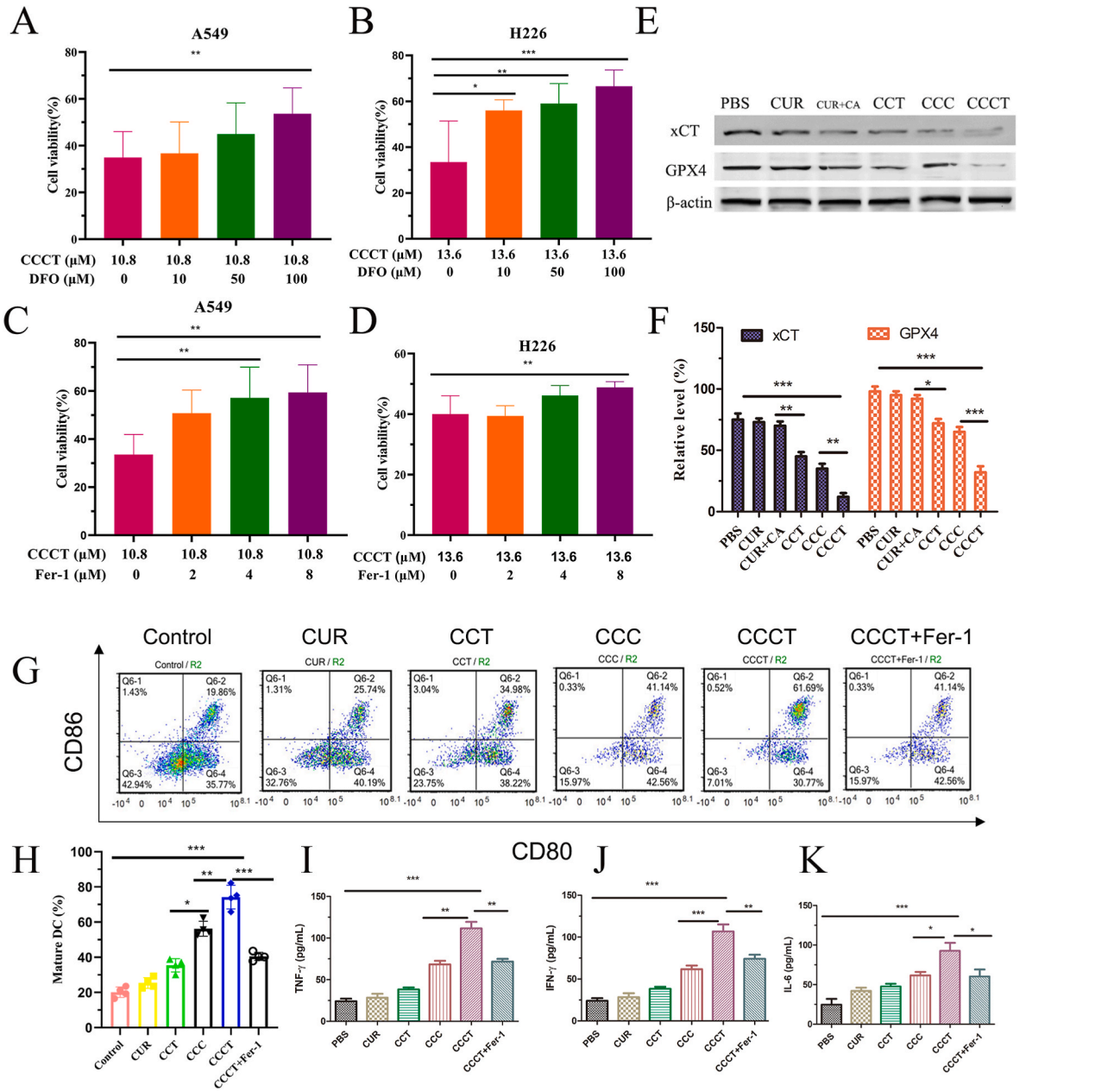

Fig. 5. CCCT-mediated ferroptosis for in vitro immune activation. The viability of A549 treated with CCCT NPs and different doses of DFO (A) and Fer-1(B) for 24 h. H226 cells treated with CCCT NPs and different doses of DFO (C) and Fer-1(D) for 24 h. All data are presented as the means ± standard deviations (n = 6); *P < 0.05, **P < 0.01, ***P < 0.001. (E) The levels of GXP4 or xCT protein by WB (n = 2). (F) Relative expression of GXP4 and xCT of A549 cells after treatment with PBS, CUR, CUR + CA, CCT, CCC, CCCT. Flow cytometry plots (G) and content (H) of matured DCs ($CD11c^{+}CD80^{+}CD86^{+}$) in lymph nodes with varying treatments. IFN- γ (I), TNF- α (J), and IL-6 (K) levels in serum of every treated mice (n = 3). The data are presented as the mean ± standard deviation; *P < 0.05, **P < 0.01, ***P < 0.001.

3.6. CCCT-mediated ferroptosis for in vitro immune activation

After investigating the mechanisms of ferroptosis in CCCT-treated tumor cells, we further examined whether CCCT-mediated ferroptosis could elicit an immune response in vitro. The maintenance of T-cell-mediated immune response involves DCs, a specialized system of antigen-presenting cells. The iDCs, upon encountering tumor antigens, will internalize and undergo antigen processing to generate peptide fragments [34]. As they migrate towards the adjacent lymphoid tissues, they undergo a process of maturation and present peptide-major histocompatibility complex molecules (MHC-I and MHC-II) to T cells, resulting in the generation of effector T cells that are responsible for eliminating tumor cells [35]. In this experiment, we employed a transwell system to co-culture A549 cells treated with CCCT NPs together with iDCs for 24 h. Next, the DCs were gathered and underwent flow cytometry analysis to assess the levels of CD86 and CD80 costimulatory molecules, which are commonly recognized as markers for DC maturation. The treatment of CCCT NPs significantly enhanced the maturation of DCs (52.8 % $CD86^+/CD80^+$, gated on $CD11c^+$ cells), demonstrating a substantial increase compared to the control group (19.1 %) (Fig. 5G). On the contrary, the presence of ferroptosis inhibitor Fer-1 significantly hindered the maturation process of DCs when co-cultured with CCCT-treated A549 cells (with a decrease to 41.9 % for Fer-1). This suggests that the induction of cell ferroptosis by CCCT NPs can effectively stimulate DC maturation. As CUR was present, they could potentially trigger ferroptosis in cancer cells [36]. Consequently, even in the absence of CA, some cancer cells that were co-cultured with CUR experienced partial cell death due to the occurrence of ferroptosis. Therefore, in the case of co-culturing A549 cancer cells treated with CCC with DCs, there is a slight enhancement observed in the maturation of DCs. The levels of DC activation-related cytokines, such as TNF-α, INF-γ and IL-6, were significantly increased when DCs were co-cultured with CCCT-treated A549 cells. This finding was consistent with the maturation of DCs (Fig. 5H–K). In combination, these indicate that the utilization of CCCT NPs effectively triggered a cellular immune response by tumor cell ferroptosis.

3.7. CCCT in vivo images of lung cancer xenografts in mice

To provide additional evidence of the targeting ability of CCCT, we conducted a distribution analysis of NPs throughout the entire body. As shown in Fig. 6A, the dispersion of CCCT loaded with DIR (CCCT/DIR) in mice. The fluorescence intensity of CCCT/DIR NPs was observed to be stronger after 8 h, potentially indicating their ability to evade lysosomes and penetrate into the cytoplasm, as compared to that of free DIR. Furthermore, the release of DIR was promptly observed when exposed to low pH and high levels of HAase, and the signal intensity continued to exhibit a robust increase for a duration of 24 h. The measurement of fluorescence intensity in major organs and tumors in mice was determined through the analysis of specific regions of interest (ROI). Fig. 6B showed the group treated with CCCT/DIR NPs exhibited the highest fluorescence signal intensity in tumor regions compared to other groups. The fluorescence intensity of the CCCT/DIR NPs was significantly higher, with a 5.76-fold increase compared to free DIR. This suggests that the CCCT NPs have an extended circulation time and enhanced targeting ability.

3.8. CCCT-mediated ferroptosis for in vivo immune system activation

To assess the in vivo efficacy of CCCT NPs against tumor growth, A549 cell xenografts were established in nude mice. As depicted in Fig. 7A–C, the use of CCCT NPs resulted in a significant reduction in A549 tumor growth compared to the control group (PBS). Notably, it exhibited the highest tumor inhibition rate (TIR) of 74.75 %, which was considerably higher than that achieved with CUR, CCT, and CCC NPs by factors of 2.5-, 1.9- and 1.5-fold respectively (Fig. 7D). These results were further supported by tumor weight measurements (Fig. 7E). Furthermore, histological examination of the tumor tissues was conducted using immunohistochemistry staining, which revealed an augmented immunoreactivity for GPX4 in the CCCT group (Fig. 7F). Concurrently, the tumor samples were subjected to histological analysis using H&E staining. The tumor tissues in the PBS, CCT and CCC groups exhibited a high cell density, as shown in Fig. 7G, indicating robust proliferation of tumor cells. In contrast, the tumor tissue of the CCCT group contained numerous nuclear fragments, suggesting significant nuclear damage. CCCT NPs augmented tumor growth inhibition by facilitating DC maturation and secreting TNF-α, IL-6, and IFN-γcytokines (Fig. 7H–L). The results from Fig. 7M demonstrated that the administration of CCCT NPs to mice did not lead to significant alterations in body weight when compared to the other groups. Furthermore, minimal systemic toxicity was confirmed through the analysis of sacrificed organs using H&E staining and hemolysis test (Fig. 7N).

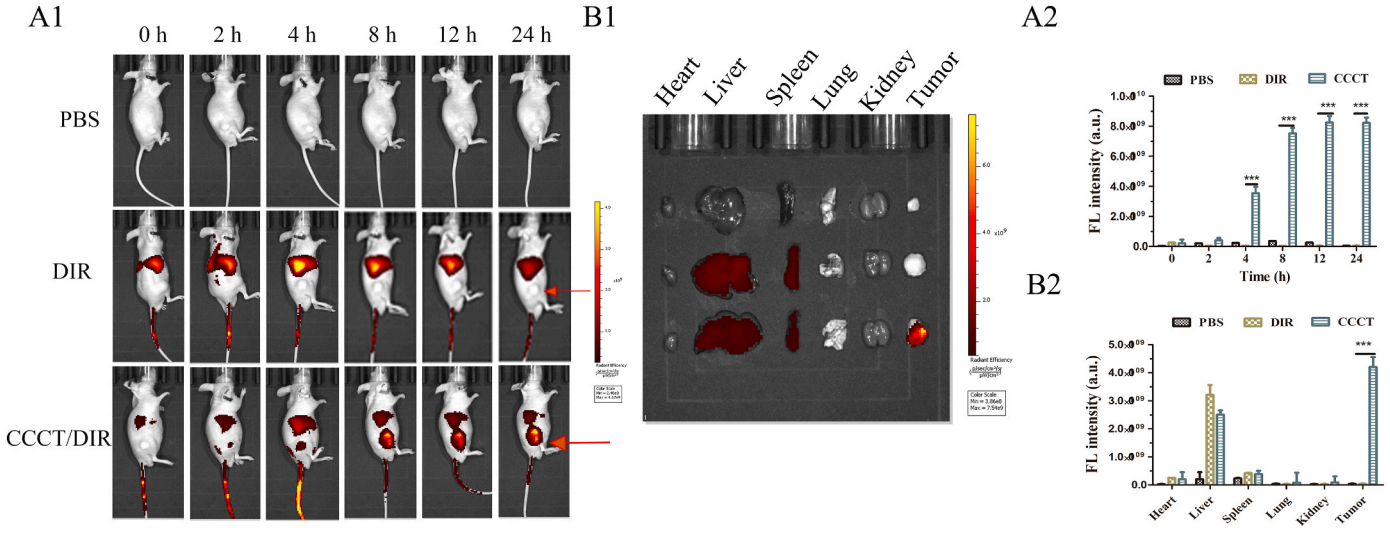

Fig. 6. Tumor target ability of every formulation in A549 cells xenografts in BALB/c mice after i.v. of PBS, DIR, CCCT NPs. (A) In vivo real-time non-invasive whole-body imaging. (B) Ex vivo fluorescence of tumors and organs isolated from A549 cells xenografts in BALB/c mice. (1) Image of the distribution of drugs in the body or tumors and organs. (2) Fluorescence intensity of image. Data are presented as the mean ± SD (n = 3). The data are presented as the mean ± standard deviation; *P < 0.05, **P < 0.01, ***P < 0.001.

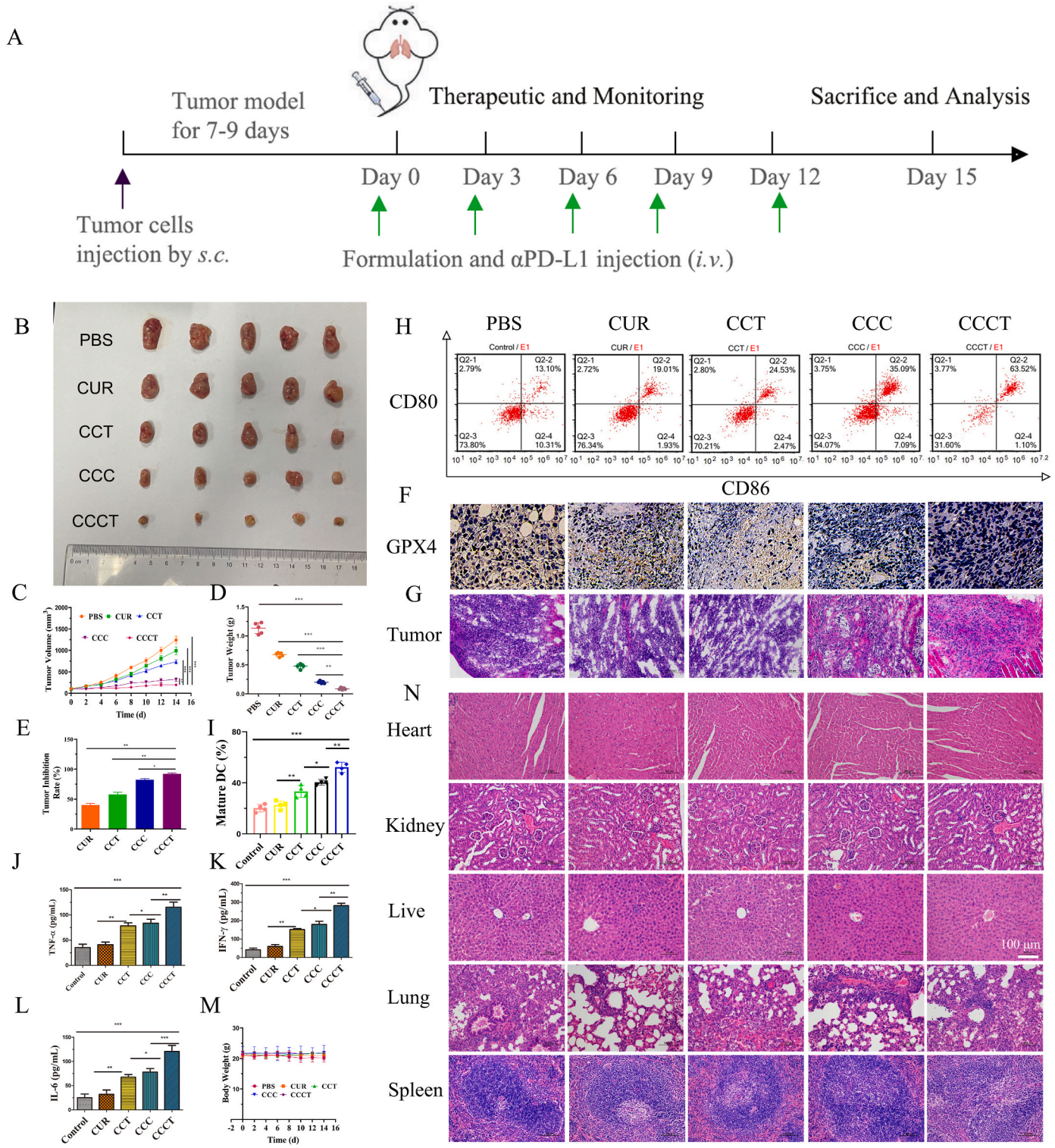

Fig. 7. CCCT-mediated ferroptosis for in vivo immune system activation. (A) Schematic illustration of dosing regimens of CCCT NPs in A549 tumor-bearing mice. Images of the tumors (B), tumor growth inhibition curves (C), and tumor weight (D) for a murine model with A549 xenografts after intravenous injection with the different formulations. (E) The tumor inhibitory rate (TIR). The TIR is calculated using the following equation: TIR (%) = [1 − X/Y] × 100 %. X, The average weights of the tumors from the experimental groups; Y, the average weights of the tumors from control groups). Flow cytometry analysis (H) and quantification (I) of mature DCs ($CD86^+/CD80^+$, gated on $CD11c^+$ cells) in the lymph nodes of A549 tumor-bearing mice at 24 h after mice received different treatments. TNF-α (J), IFN-γ (K), and IL-6 (L) secreted in the culture medium by DCs. Immunohistochemical assay of the levels of GPX4 (F), H&E staining (G), and body weight (M) and of tumor tissues of A549 xenograft-bearing nude mice treated with various formulations in vivo (n = 5). (N) H&E staining of the heart, liver, spleen, lung and kidney of the mice after treatment with every treated groups (n = 5). The data are presented as the mean ± standard deviation; *P < 0.05, **P < 0.01, ***P < 0.001.

It has been demonstrated that the enhancement of antitumor immunity can be achieved by obstructing PD-1/PD-L1 checkpoints, which effectively prevents the reduction of effector T cells [37,38]. This effect is particularly pronounced when combined with other therapeutic approaches, leading to significant improvements in antitumor efficacy [27]. Consequently, we utilized PD-1 inhibition (αPD-L1) as an additional strategy to enhance the therapeutic impact of CCCT-induced ferroptosis on tumor growth. Compared with PBS or CCCT alone, tumor weight and inflammatory cells of CCCT+αPD-L1 were significantly decrease, and tumor inhibition rate were significantly increased (Fig. 8A–D, Fig. S12). The combination of CCCT and αPD-L1 significantly augmented the maturation of DCs, surpassing that achieved by CCCT alone (Fig. 8E–F). The levels of DC activation-associated cytokines, including TNF-α, INF- γ, and IL-6, exhibited a notable rise upon treated with CCCT+αPD-L1 (Fig. 8G–I). In combination, these findings indicate that the simultaneous use of PD-1 blockade and CCCT-induced ferroptosis effectively suppressed tumor growth in vivo.

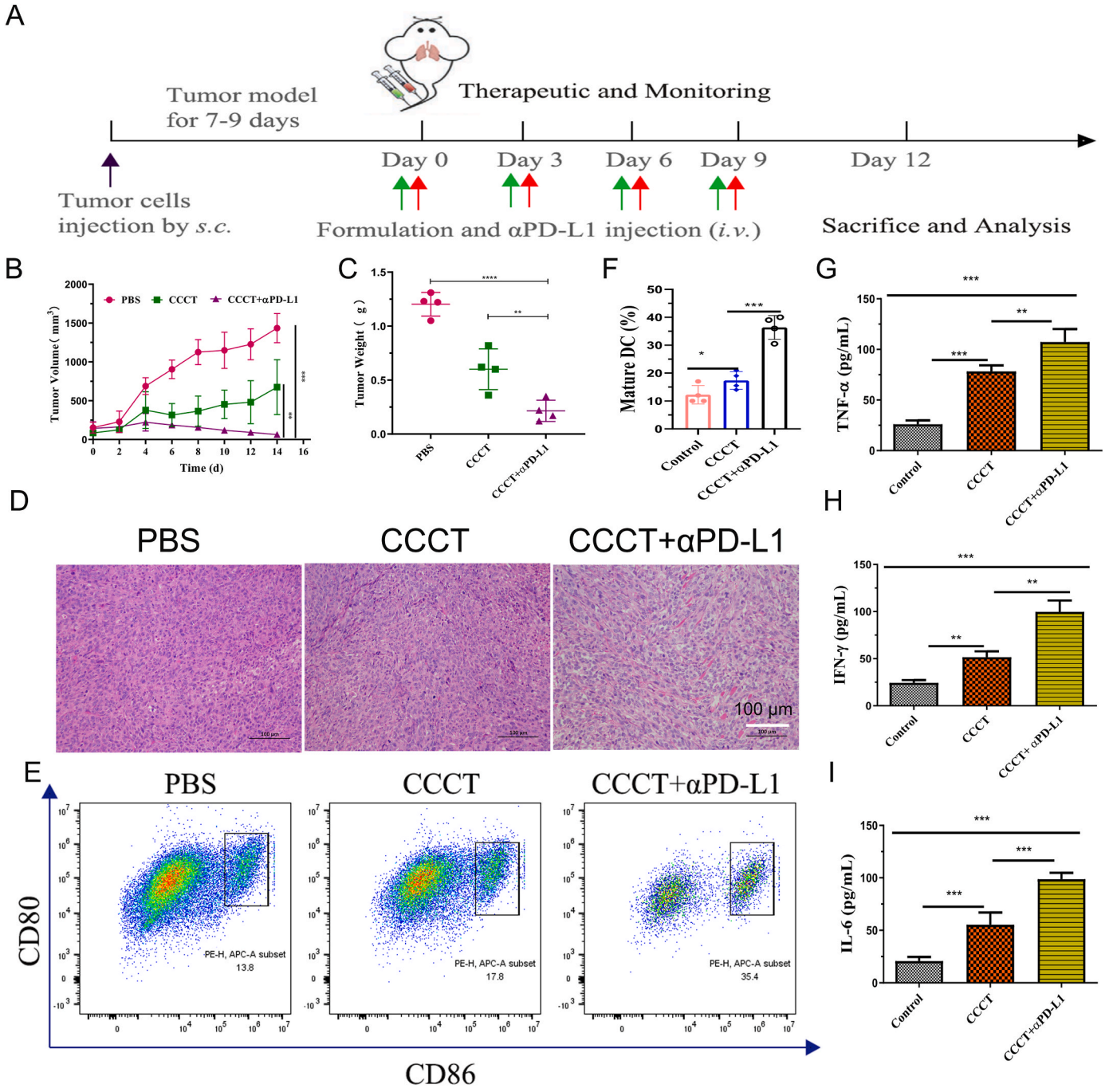

Fig. 8. CCCT-mediated ferroptosis for in vivo immune system activation. (A) Schematic illustration of dosing regimens of CCCT NPs+ αPD-L1 in A549 tumor-bearing mice. Tumor growth inhibition curves (B) and tumor weight (C) for a murine model with A549 xenografts after intravenous injection with PBS, CCCT, CCCT+ αPD-L1 formulations. (D) H&E staining of tumor tissues of A549 xenograft-bearing nude mice treated with various formulations in vivo (n = 4). Flow cytometry plots (E) and content (F) of matured DCs ($CD11c^+CD80^+CD86^+$) in lymph nodes with varying treatments. IFN- γ (G), TNF- α (H), and IL-6 (I) levels in serum of every treated mice (n = 4). The data are presented as the mean ± standard deviation; *P < 0.05, **P < 0.01, ***P < 0.001.

4. Conclusion

In brief, a CS based dual drug delivery nanoparticle (CCCT) with sequential tumor cells and mitochondria targeting function was developed to enhance the effects of ferroptosis induction and immunotherapy in lung cancer. CCCT are anticipated to achieve targeted CA and CUR delivery to tumor tissues, thereby enabling highly effective tumor inhibition while maintaining high safety. Based on physicochemical assessments, this innovative NPs exhibits excellent responsiveness in highly acid and hyaluronidase sensitive condition. Furthermore, both cellular and animal studies have demonstrated the efficacy of these NPs in cancer treatment, as well as their enhanced safety profile. In summary, these innovative CCCT NPs, which target tumor resistance to apoptosis, hold great promise for future clinical applications in cancer chemotherapy and are anticipated to make significant contributions to the field.

CRediT authorship contribution statement

He Wang: Conceptualization. **Shuimu Lin:** Data curation. **Jiacui Xie:** Methodology. **Xuming Chen:** Data curation. **Yating Deng:** Methodology. **Pei Huang:** Conceptualization. **Kanglong Peng:** Data curation. **Wenhui Gao:** Methodology. **Guodong Ye:** Software. **Guihua Wang:** Methodology. **Xiyong Yu:** Resources. **Huaying Wen:** Funding acquisition. **Linghao Qin:** Writing – original draft, Data curation. **Yi Zhou:** Writing – review & editing, Writing – original draft.

Ethics approval

The in vivo experiments were conducted in accordance with the guidelines of the Institutional Animal Care and Use Committee (IACUC) at the Animal Experiment Center of Guangzhou Medical University, China, as well as NIH Guide for the Care and Use of Laboratory Animals.

Declaration of competing interest

We declare that we have no financial and personal relationships with other people or organizations that can inappropriately influence our work, there is no professional or other personal interest of any nature or kind in any product, service and/or company that could be construed as influencing the position presented in, or the review of, the manuscript entitled “Chondroitin sulfate nanoparticles based on co-delivery dual drug induced ferroptosis in lung cancer cells by disrupting mitochondrial oxidative homeostasis”.

Acknowledgements

This study was supported by Natural Science Foundation of Guangdong Province, China (Nos. 2021A1515011367, 2023A1515010125), Guangzhou Science and technology planning project, China (2022-01-02-05-3017-0019). Guangzhou Health Science and Technology General Guidance Project, China (20221A011107). Guangzhou Science and Technology Bureau City School Joint Project, China (202201020394), Student Innovation Ability Improvement Program of Guangzhou Medical University , China(2023). Provincial-level Key Laboratory Open subject in Guangzhou Medical University, China (J24413010, 2023). Guangzhou Medical University Scientific Research Capacity Enhancement Program Project - Strong Foundation for scientific research, China (2025, He Wang , 0803030089 ; and Yi Zhou , 01-410-250241). Thanks to Professor Li Shiying for the comments on the article.

Appendix A. Supplementary data

Supplementary data to this article can be found online at https://doi.org/10.1016/j.mtbio.2025.101632.

Data availability

The data that has been used is confidential.

References

[1] A.G. Jayaprasad, et al., Int. J. Biol. Macromol. 264 (Pt 1) (2024) 130151.
[2] A. Jablonska-Trypuc, et al., Nutrients 10 (1) (2018).
[3] S. Aghazadeh, R. Yazdanparast, Apoptosis 21 (11) (2016) 1302.
[4] P. Savage, BMC Cancer 16 (1) (2016) 906.
[5] S. Raz, et al., Cell Death Dis. 5 (2) (2014) e1067.
[6] X. Yan, et al., Acta Biomater. 188 (2024) 329.
[7] D. Tang, R. Kang, Cancer drug resistance 7 (2024) 41.
[8] X. Bai, et al., Cell Death Dis. 15 (11) (2024) 819.
[9] J.P. Won, et al., Eur. J. Pharmacol. (2024) 177104.
[10] Y. Liu, et al., J. Inflamm. Res. 17 (2024) 8471.
[11] Q. Xie, et al., ACS Nano 18 (47) (2024) 32438–32450.
[12] X. Tang, et al., Thorac Cancer 12 (8) (2021) 1219.
[13] H. Chen, et al., Oxid. Med. Cell. Longev. 2023 (2023) 6896790.
[14] B. Shi, et al., Adv Healthc Mater 13 (11) (2024) e2303837.
[15] M. Meng, et al., Oncotarget 8 (44) (2017) 76385.
[16] H. Wang, et al., J Nanobiotechnology 19 (1) (2021) 152.
[17] Z. Cai, et al., Biomacromolecules 18 (6) (2017) 1677.
[18] Y. Li, et al., Carbohydr. Polym. 255 (2021) 117393.
[19] X. Shi, et al., Carbohydr. Polym. 254 (2021) 117459.
[20] D. Huang, et al., J. Med. Chem. 65 (14) (2022) 9955.
[21] J. Zielonka, et al., Chemical reviews 117 (15) (2017) 10043.
[22] B. Kalyanaraman, FASEB J. : official publication of the Federation of American Societies for Experimental Biology 36 (4) (2022) e22226.
[23] H. Wang, et al., J Nanobiotechnology 18 (1) (2020) 8.
[24] R. Zheng, et al., J Control Release 336 (2021) 159.
[25] Y. Zhou, et al., Acta Pharm. Sin. B 13 (7) (2023) 3153.
[26] P. Huang, et al., Eur J Pharm Sci 204 (2024) 106942.
[27] Q. Jiang, et al., Small 16 (22) (2020) e2001704.
[28] H. Hadji, K. Bouchemal, J Control Release 342 (2022) 93.
[29] K. Fang, et al., Adv Healthc Mater 12 (28) (2023) e2301328.
[30] X. Yi, et al., Pharmaceutics 14 (8) (2022).
[31] D. Guo, et al., Int J Pharm 666 (2024) 124744.
[32] K. Deng, et al., J Control Release 366 (2024) 684.
[33] C. Huang, et al., Eur. J. Med. Chem. 265 (2024) 116112.
[34] A. Barnwal, et al., Acs Biomater Sci Eng 9 (11) (2023) 6409.
[35] S. Zhang, et al., J Immunother Cancer 11 (7) (2023).
[36] Y. Zhang, J. Xie, Phytother Res. 38 (4) (2024) 2041.
[37] D. Fanale, et al., BMC Cancer 23 (1) (2023) 437.
[38] J. Liu, et al., Adv Mater 36 (9) (2024) e2309562.